Bibliography

Papers of special note have been highlighted as either of interest (•) or of considerable interest (••) to readers.

1. Bader H, Ringsdorf H, Schmidt B. Watersoluble polymers in medicine. Angew Chem Int Ed Engl 1984;123/124:457-85

•• **This was the first paper concerning polymeric micelle drug carrier systems.**

2. Pratten MK, Lloyd JB, Ringsdorf H. Micelle-forming block copolymers: pinocytosis by macrophages and interaction with model membranes. Makromol Chem 1985;186:725-33

3. Yokoyama M, Inoue S, Sakurai Y. Molecular design for missile drug: synthesis of adriamycin conjugated with IgG using poly(ethylene glycol)-poly (aspartic acid) block copolymer as intermediate carrier. Makromol Chem 1989;190:2041-54

4. Kabanov AV, Alakhov VY, Kabanov VA, et al. The neuroleptic activity of haloperidol increases after its solubilization in surfactant micelles: micelles as microcontainers for drug targeting. FEBS Lett 1989;258:343-5

• **This reported the first enhancement in the in vivo pharmacological activity of drug by the use of polymeric micelles.**

5. Yokoyama M, Okano T, Inoue S, et al. Toxicity and antitumor activity against solid tumors of micelle-forming polymeric drug and its extremely long circulation in blood. Cancer Res 1991;51:3229-36

•• **This reported the first case of in vivo antitumor effect enhancement by the use of polymeric micelle carriers.**

6. Kwon GS, Yokoyama M, Kataoka K, et al. Enhanced tumor accumulation and prolonged circulation times of micelle-forming poly(ethylene oxide-aspartate) block copolymer-adriamycin conjugates. J Control Release 1994;29:17-23

• **This provided the first proof of tumor targeting with polymeric micelles.**

7. Yokoyama M, Okano T, Kataoka K, et al. Selective delivery of adriamycin to a solid tumor using a polymeric micelle carrier system. J Drug Targeting 1999;7:171-86

•• **This paper clearly proved that significant antitumor effect enhancement resulted from tumor targeting effects of a polymeric micelle carrier.**

8. Batrakova EV, Alakhov VY, Kabanov AV, et al. Anthracycline antibiotics non-covalently incorporated into the block copolymer micelles: in vivo evaluation of anti-cancer activity. Br J Cancer 1996;74:1545-52

9. Kabanov AV, Alakhov VY. Micelles of amphiphilic block copolymers as vehicles for drug delivery. In: Alexandridis P, Lindman B, editors, Amphiphilic block copolymers: self assembly and applications. Elsevier, Netherlands; 1997. p. 1-31

• **A good review for biological activities of block copolymers.**

10. Yu BG, Okano T, Kwon GS, et al. Polymeric micelles for drug delivery: solubilization and haemolytic activity of amphotericin B. J Control Release 1998;53:131-6

11. Rolland A, O'Mullane J, Petrak K, et al. New macromolecular carriers for drugs. I. Preparation and characterization of poly (oxyethylene-b-isoprene-b-oxyethylene) block copolymer aggregates. J Appl Polym Sci 1992;44:1195-203

12. Inoue T, Nakamae K, Hoffman AS, et al. An AB block copolymer of oligo(methyl methacrylate) and poly(acrylic acid) for micellar delivery of hydrophobic drugs. J Control Release 1998;51:221-9

13. Zhang X, Burt HM, Hunter WL, et al. An investigation of the antitumor activity and biodistribution of polymeric micellar paclitaxel. Cancer Chemother Pharmacol 1997;40:81-6

14. Matsumura Y, Kataoka K. Preclinical and clinical studies of anticancer agent-incorporating polymer micelles. Cancer Sci 2009;100:572-9

15. Matsumura Y. Polymeric micellar delivery systems in oncology. Jpn J Clin Oncol 2008;38:793-802

16. Matsumura Y. Poly (amino acid) micelle nanocarriers in preclinical and clinical studies. Adv Drug Deliv Rev 2008;60:899-914

• **A good review of clinical studies of polymeric micelle systems.**

17. Matsumura Y, Hamaguchi T, Watanabe N, et al. Phase I clinical trial and pharmacokinetic evaluation of NK911, a micelle-encapsulated doxorubicin. Br J Cancer 2004;91:1775-81

18. Hamaguchi T, Kato K, Matsumura Y, et al. A phase I and pharmacokinetic study of NK105, a paclitaxel-incorporating micellar nanoparticle formulation. Br J Cancer 2007;97:170-6

19. Danson S, Alakhov V, Ranson M, et al. Phase I dose escalation and pharmacokinetic study of pluronic polymer-bound doxorubicin (SP1049C) in patients with advanced cancer. Br J Cancer 2004;90:2085-91

20. Kim DW, Kim SY, Heo DS, et al. Multicenter phase II trial of Genexol-PM, a novel Cremophor-free, polymeric micelle formulation of paclitaxel, with cisplatin in patients with advanced non-small-cell lung cancer. Ann Oncol 2007;18:2009-14

21. Lee KS, Chung HC, Ro J, et al. Multicenter phase II trial of Genexol-PM, a Cremophor-free, polymeric micelle formulation of paclitaxel, in patients with metastatic breast cancer. Breast Cancer Res Treat 2008;108:241-50

22. Park SR, Oh DY, Kim HK, et al. A multi-center, late phase II clinical trial of Genexol (paclitaxel) and cisplatin for patients with advanced gastric cancer. Oncol Rep 2004;12:1059-64

23. Kim TY, Kim DW, Bang YJ, et al. Phase I and pharmacokinetic study of Genexol-PM, a cremophor-free, polymeric micelle-formulated paclitaxel, in patients with advanced malignancies. Clin Cancer Res 2004;10:3708-16

24. Christian DA, Minko T, Discher DE, et al. Flexible filaments for in vivo imaging and delivery: persistent circulation of filomicelles opens the dosage window for sustained tumor shrinkage. Mol Pharm 2009;6:1343-52

25. Geng Y, Minko T, Discher DE, et al. Shape effects of filaments versus spherical particles in flow and drug delivery. Nat Nanotechnol 2007;2:249-55

26. Tuzar Z, Kratochvil P. Block and graft copolymer micelles in solution. Adv Coll Interface Sci 1976;6:201-32

27. Aliabadi M, Lavasanifar A. Polymeric micelles for drug delivery. Expert Opinion Drug Deliv 2006;3:139-62

•• **An excellent review of polymeric micelle drug carrier systems.**

28. Kwon GS. Polymeric micelles for delivery of poorly water-soluble compounds. Crit Rev Ther Drug Carrier Syst 2003;20:357-403

29. Adams ML, Lavasanifar A, Kwon GS. Amphiphilic block copolymers for drug delivery. J Pharm Sci 2003;92:1343-55
- **A good review of polymeric micelle drug carrier systems.**

30. Yokoyama M. Block copolymers as drug carriers. Crit Rev Ther Drug Carrier Syst 1992;9:213-48
- **A good review of polymeric micelle drug carrier systems focusing on polymer chemistries.**

31. Yokoyama M. Polymeric micelles for the targeting of hydrophobic drugs. In: Kwon GS, editor, Drug and pharmaceutical sciences polymeric drug delivery systems, Taylor & Francis vol. 148; 2005. p. 533-75
- **A good review of polymeric micelle drug carrier systems.**

32. Yokoyama M. Polymeric micelles as nano-sized drug carrier systems. In: Y Tabata, editor, Nanoparticles for pharmaceutical applications. American Scientific Publishers; Boca Raton 2007. p. 63-72

33. Tardi PG, Boman NL, Cullis PR. Liposomal doxorubicin. J Drug Target 1996;4:129-40

34. Gabizon AA, Shmeeda H, Zalipsky S. Pros and cons of the liposome platform in cancer drug targeting. J Liposome Res 2006;16:175-83

35. Matsumura Y, Maeda H. A new concept for macromolecular therapeutics in cancer chemotherapy: mechanism of tumoritropic accumulation of proteins and the antitumor agent smancs. Cancer Res 1986;46:6387-92
- •• **This is the original paper for the EPR effect.**

36. Maeda H, Sawa T, Konno T. Mechanism of tumor-targeted delivery of macromolecular drugs, including the EPR effect in solid tumor and clinical overview of the prototype polymeric drug SMANCS. J Control Release 2001;74:47-61

37. Maeda H, Bharate GY, Daruwalla J. Polymeric drugs for efficient tumor-targeted drug delivery based on EPR-effect. Eur J Pharm Biopharm 2009;71:409-19

38. Lorusso D, Di Stefano A, Scambia G, et al. Pegylated liposomal doxorubicin-related palmar-plantar erythrodysesthesia ('hand-foot' syndrome). Ann Oncol 2007;18:1159-64

39. Gordon KB, Tajuddin A, VonRoenn J, et al. Hand-foot syndrome associated with liposome-encapsulated doxorubicin therapy. Cancer 1995;75:2169-73

40. Negishi T, Koizumi F, Matsumura Y, et al. NK105, a paclitaxel-incorporating micellar nanoparticle, is a more potent radiosensitising agent compared to free paclitaxel. Br J Cancer 2006;95:601-6

41. Hamaguchi T, Matsumura Y, Kakizoe T, et al. NK105, a paclitaxel-incorporating micellar nanoparticle formulation, can extend in vivo antitumour activity and reduce the neurotoxicity of paclitaxel. Br J Cancer 2005;92:1240-6

42. Kim SC, Kim DW, Seo MH, et al. In vivo evaluation of polymeric micellar paclitaxel formulation: toxicity and efficacy. J Control Release 2001;72:191-202

43. Nagano T, Yasunaga M, Matsumura Y, et al. Antitumor activity of NK012 combined with cisplatin against small cell lung cancer and intestinal mucosal changes in tumor-bearing mouse after treatment. Clin Cancer Res 2009;15:4348-55

44. Kuroda J, Kuratsu J, Matsumura Y, et al. Potent antitumor effect of SN-38-incorporating polymeric micelle, NK012, against malignant glioma. Int J Cancer 2009;124:2505-11

45. Nakajima TE, Yanagihara K, Matsumura Y, et al. Antitumor effect of SN-38-releasing polymeric micelles, NK012, on spontaneous peritoneal metastases from orthotopic gastric cancer in mice compared with irinotecan. Cancer Res 2008;68:9318-22

46. Saito Y, Yasunaga M, Matsumura Y, et al. Enhanced distribution of NK012, a polymeric micelle-encapsulated SN-38, and sustained release of SN-38 within tumors can beat a hypovascular tumor. Cancer Sci 2008;99:1258-64

47. Sumitomo M, Koizumi F, Matsumura Y, et al. Novel SN-38-incorporated polymeric micelle, NK012, strongly suppresses renal cancer progression. Cancer Res 2008;68:1631-5

48. Nakajima TE, Yasunaga M, Matsumura Y, et al. Synergistic antitumor activity of the novel SN-38-incorporating polymeric micelles, NK012, combined with 5-fluorouracil in a mouse model of colorectal cancer, as compared with that of irinotecan plus 5-fluorouracil. Int J Cancer 2008;122:2148-53

49. Koizumi F, Hamaguchi T, Matsumura Y, et al. Novel SN-38-incorporating polymeric micelles, NK012, eradicate vascular endothelial growth factor-secreting bulky tumors. Cancer Res 2006;66:10048-56

50. Li Y, Kwon GS. Methotrexate ester of poly (ethylene oxide)-block-poly (2-hydroxyethyl-L-aspartamide). Part 1: effects of the level of methotrexate conjugation on the stabliity of micelles and on drug release. Pharm Res 2000;157:607-11
- **An important paper for a strategic design of polymeric micelle systems; drug release control through the control of chemically conjugated drug amount.**

51. Bae Y, Fukushima S, Kataoka K. Design of environment-sensitive supramolecular assemblies for intracellular drug delivery: polymeric micelles that are responsive to intracellular pH change. Angew Chem Int Ed Engl 2003;42:4640-3

52. Bae Y, Fukushima S, Kataoka K. Preparation and biological characterization of polymeric micelle drug carriers with intracellular pH-triggered drug release property: tumor permeability, controlled subcellular drug distribution, and enhanced in vivo antitumor efficacy. Bioconjug Chem 2005;16:122-30

53. Bae Y, Nishiyama N, Kataoka K. In vivo antitumor activity of the folate-conjugated pH-sensitive polymeric micelle selectively releasing adriamycin in the intracellular acidic compartments. Bioconjug Chem 2007;18:1131-9

54. Lee ES, Gao Z, Bae YH. Recent progress in tumor pH targeting nanotechnology. J Control Release 2008;132:164-70

55. Na K, Sethuraman VT, Bae YH. Stimuli-sensitive polymeric micelles as anticancer drug carriers. Anticancer Agents Med Chem 2006;6:525-35

56. Yokoyama M, Satoh A, Matsumura Y, et al. Incorporation of water-insoluble anticancer drug into polymeric micelles and control of their particle size. J Control Release 1998;55:219-29

57. Matsumura Y, Yokoyama M, Kakizoe T. Reduction of the adverse effects of an antitumor agent, KRN 5500 by incorporation of the drug into polymeric micelles. Jpn J Cancer Res 1999;90:122-8
- **This describes the first report concerning the *in vivo* advantages of the solubilization of a water-insoluble drug.**

58. Mizumura Y, Matsumura Y, Kakizoe T. Incorporation of the anticancer agent KRN 5500 into polymeric micelles diminishes the pulmonary toxicity. Jpn J Cancer Res 2002;93:1237-43

59. Lavasanifar A, Samuel J, Kwon GS. Block copolymer micelles for the encapsulation and delivery of amphotericin B. Pharm Res 2002;19:418-22

60. Lavasanifar A, Samuel J, Kwon GS. Micelles self-assembled from poly(ethylene oxide)-block-poly(N-hexyl stearate L-aspartamide) by a solvent evaporation method; effect on the solubilization and hemolytic activity of amphotericin B. J Control Release 2001;77:155-60

61. Yokoyama M, Opanasopit P, Okano T. Polymer design and incorporation method for polymeric micelle carrier system containing water-insoluble anti-cancer agent camptothecin. J Drug Target 2004;12:373-84

62. Opanasopit P, Yokoyama M, Okano T. Block copolymer design for camptothecin incorporation into polymeric micelles for passive tumor targeting. Pharm Res 2004;21:2003-10

63. Yokoyama M, Kwon GS, Kataoka K. Preparation of micelle-forming polymer-drug conjugates. Bioconjugate Chem 1992;3:295-301

64. Hoes CJT, Potman W, Feijen J. Optimization of macromolecular prodrugs of the antitumor antibiotic adriamycin. J Control Release 1985;2:205-13

65. Duncan R, Kopeckova-Rejmanova P, Kopecek J. Anticancer agents coupled to N-(2-hydroxypropyl)methacrylamide copolymers I. Evaluation of daunomycin and puromycin conjugates in vitro. Br J Cancer 1987;55:165-74

66. Endo N, Umemoto N, Hara T. A novel covalent modification of antibodies at their amino groups with retention of antigen-binding activity. J Immunol Methods 1987;104:253-8

67. Zunino F, Pratesi G, Micheloni A. Poly (carboxylic acid) polymers as carriers for anthracyclines. J Control Release 1989;10:65-73

68. Yamamoto T, Yokoyama M, Maitani Y, et al. What are determining factors for stable drug incorporation into polymeric micelle carriers? Consideration on physical and chemical characters of the micelle inner core. J Control Release 2007;123:11-8

69. Kabanov AV, Batrakova EV, Alakhov VY. Pluronic block copolymers for overcoming drug resistance in cancer. Adv Drug Deliv Rev 2002;54:759-79

70. Kabanov AV, Batrakova EV, Alakhov VY. An essential relationship between ATP depletion and chemosensitizing activity of Pluronic block copolymers. J Control Release 2003;91:75-83

71. Sharma AK, Zhang L, Li S, et al. Prevention of MDR development in leukemia cells by micelle-forming polymeric surfactant. J Control Release 2008;131:220-7

72. Yokoyama M, Inoue S, Sakurai Y, et al. Preparation of adriamycin-conjugated poly (ethylene glycol)-poly(aspartic acid) block copolymer. A new type of polymeric anticancer agent. Makromolekulare Chem Rapid Commun 1987;8:431-5

73. Yokoyama M, Miyauchi M, Inoue S, et al. Characterization and anti-cancer activity of micelle-forming polymeric anti-cancer drug, adriamycin-conjugated poly (ethylene glycol)-poly(aspartic acid) block copolymer. Cancer Res 1990;50:1693-700

74. Yokoyama M, Okano T, Inoue S, et al. Toxicity and antitumor activity against solid tumors of micelle-forming polymeric drug and its extremely long circulation in blood. Cancer Res 1991;51:3229-36

75. Kwon GS, Yokoyama M, Kataoka K, et al. Enhanced tumor accumulation and prolonged circulation times of micelle-forming poly(ethylene oxide-aspartate) block copolymer-adriamycin conjugates. J Control Release 1994;29:17-23

76. Yokoyama M, Okano T, Fukushima S, et al. Selective delivery of adriamycin to a solid tumor using a polymeric micelle carrier system. J Drug Targeting 1999;7:171-86

77. Yokoyama M, Okano T, Kataoka K, et al. Improved synthesis of adriamycin-conjugated poly(ethylene oxide)-poly(aspartic acid) block copolymer and formation of unimodal micellar structure with controlled amount of physically entrapped adriamycin. J Control Release 1994;32:269-77

78. Yokoyama M, Fukushima S, Okano T, et al. Characterization of physical entrapment and chemical conjugation of adriamycin in polymeric micelles and their design for in vivo delivery to a solid tumor. J Control Release 1998;50:79-92

79. Nakanishi T, Matsumura Y, Yokoyama M, et al. Development of the polymer micelle carrier system for doxorubicin. J Control Release 2001;74:295-302

80. Tsukioka Y, Matsumura Y, Kakizoe T, et al. Pharmaceutical and biomedical differences between micellar doxorubicin (NK911) and liposomal doxorubicin (Doxil). Jpn J Cancer Res 2002;93:1145-53

81. Kawaguchi T, Yamamoto T, Yokoyama M, et al. Histological study on side effects and tumor targeting of a block copolymer micelle on rats. J Control Release 2009;136:240-6

- **Histological study concerning toxicities of a block copolymer.**

82. Opanasopit P, Y Maitani, T Okano, et al. Influence of serum and albumins from different species on stability of camptothecin-loaded micelles. J Control Release 2005;104:313-21

83. Watanabe M, Yokoyama M, Maitani Y, et al. Preparation of camptothecin-loaded polymeric micelles and evaluation of their incorporation and circulation stability. Int J Pharm 2006;308:183-9

84. Kawano K, Yokoyama M, Maitani Y, et al. Enhanced antitumor effect of camptothecin loaded in long-circulating polymeric micelles. J Control Release 2006;112:329-32

85. Hayama A, Kawano K, Maitani Y, et al. Polymeric micelles modified by folate-PEG-lipid for targeted drug delivery to cancer cells in vitro. J Nanosci Nanotechnol 2008;8:3085-90

86. Kawakami S, Opanasopit P, Hashida M, et al. Biodistribution characteristics of all-trans retinoic acid incorporated in liposomes and polymeric micelles following intravenous administration. J Pharm Sci 2005;94:2606-15

87. Chansri N, Kawakami S, Hashida M, et al. Anti-tumor effect of all-trans retinoic acid loaded polymeric micelles in solid tumor bearing mice. Pharm Res 2008;25:428-34

88. Okuda T, Kawakami S, Hashida M, et al. Block copolymer design for stable encapsulation of N-(4-hydroxyphenyl) retinamide into polymeric micelles in mice. Int J Pharm 2008;357:318-22

89. Okuda T, Kawakami S, Hashida M, et al. Enhanced in vivo antitumor efficacy of fenretinide encapsulated in polymeric micelles. Int J Pharm 2006;373:100-6

90. Satoh T, Kagechika H, Yokoyama M, et al. Encapsulation of the synthetic retinoids Am80 and LE540 into polymeric micelles and the retinoids' release control. J Control Release 2009;136:187-95

91. Koide H, Yokoyama M, Oku N, et al. Particle size-dependent triggering of accelerated blood clearance phenomenon. Int J Pharm 2008;362:197-200

92. Dams ET, Storm G, Boerman OC, et al. Accelerated blood clearance and altered biodistribution of repeated injections of sterically stabilized liposomes. J Pharmacol Exp Ther 2000;292:1071-9

• **The first report of the ABC phenomenon.**

93. Laverman P, Carstens MG, Storm G, et al. Factors affecting the accelerated blood clearance of polyethylene glycol-liposomes upon repeated injection. J Pharmacol Exp Ther 2001;298:607-12

94. Ishida T, Ichihara M, Kiwada H, et al. Spleen plays an important role in the induction of accelerated blood clearance of PEGylated liposomes. J Control Release 2006;115:243-50

95. Ishida T, Kiwada H. Accelerated blood clearance (ABC) phenomenon upon repeated injection of PEGylated liposomes. Int J Pharm 2008;354:56-62

96. Nishiyama N, Matsumura Y, Kataoka K, et al. Novel cisplatin-incorporated polymeric micelles can eradicate solid tumors in mice. Cancer Res 2003;63:8977-83

97. Uchino H, Matsumura Y, Kakizoe T, et al. Cisplatin-incorporating polymeric micelles (NC-6004) can reduce nephrotoxicity and neurotoxicity of cisplatin in rats. Br J Cancer 2005;93:678-87

Affiliation

Masayuki Yokoyama PhD
Associate Professor,
Jikei University School of Medicine,
Research Center for Medical Science,
Medical Engineering Laboratory,
3-25-8, Nishi-shinbashi,
Minato-ku, Tokyo 105-8461, Japan
Tel: +81 3 3433 1111 ext. 2336;
Fax: +81 3 3459 6005;
E-mail: masajun2093ryo@jikei.ac.jp

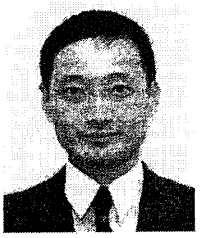

高分子ミセルの薬剤学分野への応用

横 山 昌 幸* Masayuki Yokoyama
東京慈恵会医科大学総合医科学研究センター医用エンジニアリング研究室

1. はじめに

高分子ミセルの薬物キャリヤーとしての研究は1980年代に始まったもので[1~3]，薬物キャリヤーとしては新しい部類に入るであろう．よって，読者にとって馴染みがなかったり，薬物キャリヤーとしての検討が余りなされていない部分があるのが現状である．一方で，抗がん剤を内包したDDSシステムの臨床試験が2000年代から始まり[4]，現在，世界で6件の臨床試験が行われている．現時点では，その研究・開発はまだ熱しているとは言えないが，臨床試験の結果などによっては今後大きく発展する余地があるのが，高分子ミセル薬物キャリヤーと言えよう．

以上の状況下で，高分子ミセル薬物キャリヤーの特徴を製剤学的な観点からまとめておくことは意義があると思う．特に，余り書かれることの少ない(短所については原著論文の種になりにくいため，記述されることが少ないので）高分子ミセルキャリヤーの短所についてまとめることは重要と思われる．

2. 高分子ミセルとは[5~8]

「高分子ミセル」とはその名の通り，高分子から成るミセル構造のことである．ある高分子の中に溶媒に溶けやすい部分（ここではAとする）と，その溶媒中で会合する高分子鎖（Bとする）が共存した場合に，Bの部分が会合して形成する構造がミセルである．この会合力として一般的なのは疎水性相互作用である．封入する薬物が疎水性である場合が多いためで，典型的な高分子ミセルキャリヤーではB鎖は疎水性鎖になる．その他には静電相互作用によってミセル形成及び薬物封入がなされるが，封入対象が核酸やタンパク質のように高分子で荷電密度が高いものの場合だけである．

図1にAB型ブロックコポリマーからなる高分子ミセル型薬物キャリヤーシステムの例を示す．これは直鎖状の高分子鎖であるA鎖とB鎖が直列につながった形のブロックコポリマーであり，高分子ミセル型薬物キャリヤーシステムとして最も典型的なものである．水溶性のA鎖としては，ポリエチレングリコール（PEG）が用いられることが圧倒的に多い．このAB型ブロックコポリマーが，数十～数百個会合してB鎖が疎水性の内核を，A鎖は親水性の外殻を構成した球状のミセル構造を形成する．ミセルに導入する薬物は，B鎖に化学的に結合するか，B鎖が形成するミセル内核に物理的に主に疎水性相互作用で封入される．

低分子両親媒性脂質から成るミセル構造の場合に知られているように，ミセルには大別すると球状ミセルと棒状ミセルがある．高分子ミセルの場合にも，棒状のミセルが薬物キャリヤーとしての検討が始められたが[9]，本総説は球状ミセルのみを扱う．

高分子科学での高分子ミセルに関する基礎研究の歴史は古く，1970年代にはすでにかなり広範に研究がなされていたが[10]，薬物キャリヤーとして応用する研究は，1984年[1]になって開始されたものである．その歴史については，参考文献[6,7]を参照されたい．

*1984年東京大学工学部合成化学科卒業．東京女子医科大学，(財)神奈川科学技術アカデミーでの勤務を経て2009年4月から現職．研究テーマは機能性高分子を用いたDDS，バイオマテリアル．近年は，科学不正の歴史と科学倫理実践にも興味をもつ．趣味は野球観戦，写真．連絡先：〒105-8461 東京都港区西新橋3-25-8
E-mail: masajun2093ryo@jikei.ac.jp

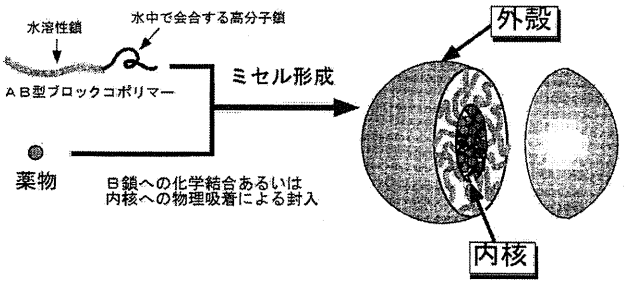

図1　高分子ミセル薬物キャリヤーシステムの構築

表1　高分子ミセル薬物キャリヤーとしての特徴

特長	
	1. ナノサイズの小さな粒径（10～100 nm）
	2. ミセル構造の高い安定性
	3. 様々なタイプの薬物封入が可能
	4. 低い毒性
	5. 機能的な材料設計が容易
短所	
	1. 比較的高度な高分子合成が必要
	2. 薬物封入法が未発達

3. 高分子ミセルの特長

高分子ミセル薬物キャリヤーシステムの特長と短所を表1にまとめた．本項では特長を説明する．

3.1　ナノサイズの小さな粒径

球状の高分子ミセルでは，その直径が10～100 nm の範囲内で得られる．高分子ミセルとしてはこの範囲の粒径が得られることは通常のことであるが，一般的にこのナノサイズの範囲の微粒子を得ることは技術的に困難が伴う．よって，小さな粒径の粒子を得る方法として，高分子ミセルが優れている側面がある．また，その粒径分布も比較的狭いものとなる．例えば動的光散乱で測定した重量換算平均粒径±標準偏差が50±10 nm といった値である（標準偏差は用いるブロックコポリマーの分子量分布等によって増減する）．

また，粒径に関する大きな特長として，これらの粒径はミセル形成操作のみで得られ，粒径をそろえる後操作の必要がないことである．逆に，リポソームで行われているようにエクストルージョンによって粒径を小さくできないとの報告がある[11]．これは薬物キャリヤーとして用いる高分子ミセルの内核が固体状態の硬いものであるためと考えられる．

上記のような小さな粒径であることは，フィルターろ過による容易な滅菌操作を可能とし，製剤上の大きな利点となっている（もちろんこれはミクロンサイズあるいはそれに近い粒径の凝集が形成しないように，高分子組成と封入の量が適切に選択されていることが前提である）．

ドラッグターゲティングに関してこの範囲の粒径は，固形がん組織へのターゲティングなどで有用な大きさである．その理由は，この粒径であると腎臓からの排出を逃れ，かつ肝臓・脾臓の細網内皮系に捕捉されにくいために，血中循環性を高く保つことが可能である．また，固形がん組織へのパッシブターゲティングの1つの方法であるEPR 効果が利用できることである．がん組織血管の透過性亢進と，リンパ系による排出抑制によって，ナノサイズのキャリヤーは本質的に固形がん部位に選択的に蓄積しやすい性質がある．この性質はEPR 効果（Enhanced Permeability and Retention effect）と呼ばれ，1986年に前田，松村によって提唱された[12,13]．EPR 効果は，高分子ミセルに限らずに，リポソームや合成高分子の固形がんへのターゲティングにも適用されているが，これらのキャリヤーの中で高分子ミセルは，このEPR 効果を利用した疎水性の強い抗がん剤ターゲティングキャリヤーとして大変優れていると考えられる．なぜなら，EPR効果を示すためにはその大きさが5 nm～200 nm であることが求められるとともに，その表面は親水的で荷電においては中性か弱く負に帯電していることが必要である[14]．高分子ミセルでは，疎水性や正荷電の薬物を多量に封入しても疎水性内核を親水性の外殻がとり囲んでいるので，表面物性は親水的であり，EPR効果発現のための条件を満たしているからである．

3.2　ミセル構造の高い安定性

高分子ミセルは高分子の会合によって形成しているために，ターゲティングのキャリヤーとして有用であるためには，血液中でターゲティングに必要な期間ミセル構造が安定に保たれる必要がある．一般的に低分子界面活性剤から成るミセルに比べ，高分子ミセル構造は安定である．その高い安定性はミセル内核が高分子鎖間の複雑な絡み合い，相互作用により構築されていることに起因し，静的（低い臨界ミセル濃度）及び動的（小さなミセル解離速度定数）な両側面で高い安定性を有することが高分子ミセルシステムの特長である．静的な側面では，高分子ミ

セルの臨界ミセル濃度の典型的な値は1～10 μg/mLと小さく，血液中でも高分子濃度を臨界ミセル濃度より高い濃度で投与することが可能となる．

一方，動的な安定性を記述する解離速度定数はミセル構造が1本の高分子鎖に解離する速度であり，生体内では臨界ミセル濃度よりも重要な因子であるように考えられる．その理由は，生体には血液中の高分子濃度を下げる要因が多数有り（尿排泄や，各種マクロファージによる貪食など），ミセル構造の濃度を高く保つには，ミセル内核を硬い性質の高分子で構成して解離速度を小さくすることが有効と考えられるからである．但し，これまでの研究で静的な安定性と動的な安定性のどちらがどのくらい重要であるかを定量的に扱った報告はない．

3.3 様々なタイプの薬物封入が可能

前項目までは，疎水性のミセル内核に疎水性の低分子薬物を封入するタイプを中心に説明を行ってきた．薬物には疎水性部分を含むものが多いので，疎水性相互作用を利用することが最も適用範囲が広いためである．しかし，「はじめに」に記述したように高分子ミセルを形成する性質（ミセル内核の会合を生み出す相互作用）は疎水性相互作用に限定されない．水系の溶媒中，内核でB鎖が会合を起こすような相互作用を起こせばミセル形成し得るということである．疎水性相互作用の他に，静電相互作用，水素結合などこの相互作用に該当する．静電相互作用，水素結合を利用すれば，DNAやタンパク質などの高分子をミセルに封入することに応用される．また，金属錯体の抗がん剤であるシスプラチンを結合させた高分子ミセルシステム[15,16]がある．結合させたシスプラチン自身，ある程度の疎水性を有するが，ミセル形成の中心的な役割を果たしているのが高分子鎖間の架橋構造であることが他の場合と異なっている．シスプラチン分子中心の白金イオンに複数の高分子側鎖が配位結合して，高分子間に架橋構造が生ずることでミセル内核が形成している．

3.4 低い毒性

まず，高分子ミセルキャリヤー自体の生体内毒性について詳細に解明されたわけではく，表2に示す6つの臨床試験[4,17~19]が行われている現時点までで，大きな問題となっている副作用がないという現状であるということをまずお断りしておく．その上で，概念的な高分子ミセルの毒性の低さから説明させていただく．

EPR効果を利用した固形がんターゲティングでは，血液中での循環性を高めるためには腎臓のろ過作用によって排出されない充分な大きさのキャリヤーサイズである必要がある．この要件を満たしたキャリヤーは一方において，生体外へ排出されないことによる長期に蓄積毒性の懸念がある．もちろん，肝臓からの胆汁排泄の経路もあるのであるが，腎臓からの排泄が確保されていることは，現時点では重要なことと考えられている．高分子ミセルのように会合性でない材料では，高い血液循環性と長期的な腎臓からの排出性を両立するには，材料を生体内分解性とする必要がある．一方，高分子ミセルは，高分子の会合によってミセル構造が構築されているので，血液循環性が必要な期間にはミセル構造によって腎臓からの排出を免れ，長期的には高分子ミセルは1本1本の高分子鎖に解離する用に設計することが可能である．この設計では，蓄積毒性を及ぼす心配が概念上ないことになる．このためには，ブロックコポリマーの分子量を約3万以下にすればよい．

次に，筆者が研究・開発に関係したシステムについての毒性について述べる．まず，マウスがんモデルを用いた評価では，最大耐量を基準に評価を行うため，非選択的に正常組織・臓器に分布した抗がん剤による副作用が顕著に起きている状態での評価であり，高分子ミセルキャリヤー自体の毒性を評価することは困難な場合が多い．このような限られた範

表2 抗がん剤含有高分子ミセルの臨床試験

薬剤名	封入抗がん剤	主目的	段階	開発会社
NK-911	Doxorubicin	固形がんターゲティング	Phase II	日本化薬（株）
NK-105	Paclitaxel	固形がんターゲティング	Phase II	日本化薬（株）
NC-6004	Cisplatin	固形がんターゲティング	Phase I	ナノキャリア（株）
NK-012	SN-38	固形がんターゲティング	Phase I	日本化薬（株）
Genexol-PM	Paclitaxel	薬剤の可溶化	Phase II	Samyang., 韓国
SP-1049C	Doxorubicin	多剤薬剤耐性克服	Phase II	Supratek Pharma, Inc., カナダ

囲の評価であっても，内包する抗がん剤が元々有していた副作用と異なるタイプの副作用が見られるかは大切な事項である．これまでの検討ではそのような副作用は観察されることはなかった[20,21]．但し，最近の検討[22]では病的な変化はないものの，肝臓，脾臓のマクロファージなどのMPSの活性化が観察された．抗がん剤を内包する高分子ミセルでは，その殺細胞活性によってこれらの活性化は観察されないが，高分子ミセルを殺細胞性の抗がん剤よりマイルドな薬物に適用する場合には，このようは高分子ミセルキャリヤーの生体への作用は十分検討する意義のあることと考えられる．

薬物ターゲティングの臨床では，キャリヤー自体，あるいはキャリヤーによるターゲティングの特性によって元来の抗がん剤にはない特有の副作用が報告されている．リポソーム製剤におけるHand and foot syndromeであり[23,24]，抗体製剤におけるinfusion-related reactionがよく知られた例である．これまでに明らかになった高分子ミセル抗がん剤の臨床報告[18,19]では，キャリヤーシステム特有の副作用は観察されていない．

以上の結果をもって，「高分子ミセルキャリヤーには毒性はない」とか「抗がん剤を対象とした場合には全く問題はない」と言うことはできず，更なる基礎的・臨床的な検討の積み上げが必要である．しかし，少なからず行われた動物実験・臨床試験の中でキャリヤー特有の毒性が認められないという事実は，毒性面から見た高分子ミセル（あるいは広義に合成高分子キャリヤー）の高いポテンシャルを示していると考えられる．

3.5 機能的な材料設計が容易

図1に示したように，ブロックコポリマーのA鎖がミセル内核を形成し，B鎖が内核を形成する．ミセル外殻はタンパク質や細胞などの生体成分と相互作用を通して体内動態・分布を決定する．一方，内核は薬物を封入しそれを放出することで，薬効発現の役割を担う．すなわち，ブロックコポリマーのそれぞれの鎖に合目的な機能を与え，それを最適化するように化学構造を選択することが可能となる．このように，機能分離性はシステム設計の観点からみると大きな利点となり，内核を構成する高分子鎖と外殻を構成する高分子鎖とに薬物キャリヤーシステムとして必要とされる機能を分割して付与することで，より高性能のシステムが達成可能となる．

4. 高分子ミセルの短所

次に高分子ミセルキャリヤーの短所と考えられる2つの事項を述べる．

4.1 比較的高度な高分子合成が必要

典型的な高分子ミセルを得るためには，合成高分子としては一般的ではない部類のブロックコポリマーが必要であり，ブロックコポリマーの合成には比較的高度な高分子合成技術が必要とされる場合が多い．この必要性に関する説明は他の総説[25]に譲る．

また，単に高分子ミセルを形成すれば必ず薬物キャリヤーとして有用というわけではなく，ブロックコポリマーの化学構造にかなり左右されることも[26]，高分子合成化学が重要であることを示している．逆に見ると，高分子合成化学の技術がない環境での高分子ミセルキャリヤー研究・開発が遂行しにくいということであり，大きな進歩を得るためには短所であると考えられる．

4.2 薬物封入法が未発達

マイクロスフィアやリポソームなど研究と開発の歴史が長いキャリヤーシステムに比べて，新しい高分子ミセルでは，薬物を安定にかつ高効率でミセル内核に封入する方法[8,27~29]についての検討が未発達である．また，実験室でのスケールではうまく封入できても，それを臨床に向けたスケールに大きくする方法論も今後進歩させる必要を感じる．

5. おわりに

本総説では，高分子ミセル薬物キャリヤーの製剤的な特徴に述べた．本キャリヤーシステムは，水溶性高分子，リポソームなど他のキャリヤーシステムにはないいくつかの特徴があることを述べた．また，比較的に高度な高分子合成が必要なことなど，急速な発展を阻害する要因についても述べた．それにもかかわらず，DDSで果たし得る大きな可能性を考慮すれば，技術的な困難を克服して研究・開発する価値のあるキャリヤーシステムであると信じる．

引用文献

1) H. Bader, H. Ringsdorf , B. Schmidt, Watersoluble polymers in medicine, *Angew Chem.*, **123/124**, 457–485 (1984).
2) M. Yokoyama, S. Inoue, Y. Sakurai, *et al.*, Prepa-

ration of adriamycin-conjugated poly(ethylene glycol)-poly(aspartic acid) block copolymer, A new type of polymeric anticancer agent, *Die Makromolekulare Chemie Rapid Communications*, **8**, 431–435 (1987).
3) A.V. Kabanov, V.Y. Alakhov, V.A. Kabanov, *et al.*, The neuroleptic activity of haloperidol increases after its solubilization in surfactant micelles: Micelles as microcontainers for drug targeting, *FEBS Lett.*, **258**, 343–345 (1989).
4) Y. Matsumura, K. Kataoka, Preclinical and clinical studies of anticancer agent-incorporating polymer micelles, *Cancer Sci.*, **100**, 572–579 (2009).
5) M. Yokoyama, Block copolymers as drug carriers, *Crit. Rev. Ther. Drug Carrier Systems*, **9**, 213–248 (1992).
6) M. Yokoyama, Polymeric micelles for the targeting of hydrophobic drugs, In G.S. Kwon, ed., Drug and Pharmaceutical Sciences, Vol. 148, Polymeric Drug Delivery Systems, Taylor & Francis, pp. 533–575, 2005.
7) M. Yokoyama, Polymeric micelles as nano-sized drug carrier systems, In Y. Tabata, ed., Nanoparticles for Pharmaceutical Applications, American Scientific Publishers, 63–72, 2007.
8) M. Aliabadi, A. Lavasanifar, Polymeric micelles for drug delivery, *Expert Opinion Drug Delivery*, **3**, 139–162 (2006).
9) Y. Geng, T. Minko, D.E. Discher, *et al.*, Shape effects of filaments versus spherical particles in flow and drug delivery, *Nat. Nanotechnol.*, **2**, 249–255 (2007).
10) Z. Tuzar, P. Kratochvil, Block and graft copolymer micelles in solution, *Adv. Coll. Interface Sci.*, **6**, 201–232 (1976).
11) M. Yokoyama, A. Satoh, Y. Matsumura, *et al.*, Incorporation of water-insoluble anticancer drug into polymeric micelles and control of their particle size, *J. Control. Release*, **55**, 219–229 (1998).
12) Y. Matsumura, H. Maeda, A new concept for macromolecular therapeutics in cancer chemotherapy: Mechanism of tumoritropic accumulation of proteins and the antitumor agent smancs, *Cancer Res.*, **46**, 6387–6392 (1986).
13) H. Maeda, T. Sawa, T. Konno, Mechanism of tumor-targeted delivery of macromolecular drugs, including the EPR effect in solid tumor and clinical overview of the prototype polymeric drug SMANCS, *J. Control. Release*, **74**, 47–61 (2001).
14) 横山昌幸, ナノ粒子とドラッグターゲティング, 機能材料, **22**, 22–27 (2002).
15) M. Yokoyama, Y. Sakurai, K. Kataoka, *et al.*, Introduction of cisplatin into polymeric micelle, *J. Control. Release*, **39**, 351–356 (1996).
16) N. Nishiyama, Y. Matsumura, K. Kataoka, *et al.*, Novel cisplatin-incorporated polymeric micelles can eradicate solid tumors in mice, *Cancer Res.*, **63**, 8977–8983 (2003).
17) Y. Matsumura, Poly (amino acid) micelle nanocarriers in preclinical and clinical studies, *Adv. Drug Deliv. Rev.*, **60**, 899–914 (2008).
18) Y. Matsumura, T. Hamaguchi, N. Watanabe, *et al.*, Phase I clinical trial and pharmacokinetic evaluation of NK911, a micelle-encapsulated doxorubicin, *Br. J. Cancer*, **91**, 1775–1781 (2004).
19) T. Hamaguchi, K. Kato, Y. Matsumura, *et al.*, A phase I and pharmacokinetic study of NK105, a paclitaxel-incorporating micellar nanoparticle formulation, *Br. J. Cancer*, **97**, 170–176 (2007).
20) M. Yokoyama, T. Okano, S. Inoue, *et al.*, Toxicity and antitumor activity against solid tumors of micelle-forming polymeric drug and its extremely long circulation in blood, *Cancer Res.*, **51**, 3229–3236 (1991).
21) M. Yokoyama, T. Okano, S. Fukushima, *et al.*, Selective delivery of adriamycin to a solid tumor using a polymeric micelle carrier system, *J. Drug Targeting*, **7**, 171–186 (1999).
22) T. Kawaguchi, T. Yamamoto, M. Yokoyama, *et al.*, Histological study on side effects and tumor targeting of a block copolymer micelle on rats, *J. Control. Release*, **136**, 240–246 (2009).
23) D. Lorusso, A. Di Stefano, G. Scambia, *et al.*, Pegylated liposomal doxorubicin-related palmar-plantar erythrodysesthesia ('hand-foot' syndrome), *Ann. Oncol.*, **18**, 1159–1164 (2007).
24) K.B. Gordon, A. Tajuddin, J. VonRoenn, *et al.*, Hand-foot syndrome associated with liposome-encapsulated doxorubicin therapy, *Cancer*, **75**, 2169–2173 (1995).
25) 横山昌幸, 薬物キャリアに用いられる高分子材料, 特集 DDS に利用される高分子化学, *Drug Delivery System*, **23**, 610–617 (2008).
26) T. Yamamoto, M. Yokoyama, Y. Maitani, *et al.*, What are determining factors for stable drug incorporation into polymeric micelle carriers? Consideration on physical and chemical characters of the micelle inner core, *J. Control. Release*, **123**, 11–18 (2007).
27) G.S. Kwon, M. Yokoyama, T. Okano, *et al.*, Block copolymer micelles as vehicles for hydrophobic drugs, *Colloids and Surfaces, B: Biointerfaces*, **2**, 429–434 (1994).
28) M. Yokoyama, T. Okano, K. Kataoka, *et al.*, Improved synthesis of adriamycin-conjugated poly (ethylene oxide)-poly(aspartic acid) block copolymer and formation of unimodal micellar structure with controlled amount of physically entrapped adriamycin, *J. Control. Release*, **32**, 269–277 (1994).
29) M. Yokoyama, P. Opanasopit, T. Okano, *et al.*, Polymer design and incorporation method for polymeric micelle carrier system containing water-insoluble anti-cancer agent camptothecin, *J. Drug Targeting*, **12**, 373–384 (2004).

High Resolution Brain Imaging with Combined Parallel-hole and Pinhole Collimation

Qiu Huang, *Member*, Tsutomu Zeniya, Hiroyuki Kudo, Hidehiro Iida, and Grant T. Gullberg, *Fellow, IEEE*

Abstract– A brain single photon emission computed tomography (SPECT) imager is simulated for obtaining high resolution brain scans for diagnosing brain ischemia. In this simulation the camera consists of one large field of view detector with parallel-hole collimation and a smaller field of view high resolution detector with pinhole collimation. The parallel-hole collimated detector images the whole brain and acquires data without truncation. It localizes areas of particular diagnostic interest, and also provides support information for the reconstruction of data acquired by the pinhole collimated detectors. The pinhole collimated detector images small regions of the brain. It provides high resolution truncated projections, from which a high resolution region of interest (ROI) is obtained. The reconstruction is performed using a maximum a posteriori (MAP) estimate with total variation regularization within the ROI. The low resolution image from the parallel-hole collimated detector is used as prior information. This improves the quantitation for the interior problem. The combination of a large field of view parallel-hole collimated detector and a smaller field of view high resolution pinhole detector improves the quantitation in the simulated brain imaging study. It makes use of the high sensitivity of the pinhole collimator while compensates for the degradation in the reconstructed image due to interior problem caused by the small field of view of the pinhole collimator. Our simulations show potential for clinical application, where the quantitation of cerebral blood flow (CBF) and cerebral vascular reactivity (CVR) are valuable in diagnosis of ischemia, and the quantitation of benzodiazepine receptor density is important in evaluating neuronal damage due to ischemic effects.

I. INTRODUCTION

The quantitation of cerebral blood flow (CBF) and cerebral vascular reactivity (CVR) are valuable in diagnosis of ischemia, and the quantitation of benzodiazepine receptor density is important in evaluating neuronal damage due to ischemic effects. To better evaluate cerebral autoregulation, the Department of Investigative Radiology at the National Cardiovascular Center Research Institute in Osaka, Japan is designing a high resolution single photon emission computed tomography (SPECT) imager for obtaining high resolution brain. The camera consists of one large field of view detector imaging the whole brain and multiple smaller field of view high resolution detectors imaging small regions of the brain (see Fig. 1). The large field of view detector provides images without truncation that localize areas of particular diagnostic interest and provide support information for the reconstruction of high resolution regions of interest (ROIs) from high resolution truncated projections obtained with the small field of view detectors. The work presented in this paper provides simulations which show that the camera improves the quantitation for the interior reconstruction problem.

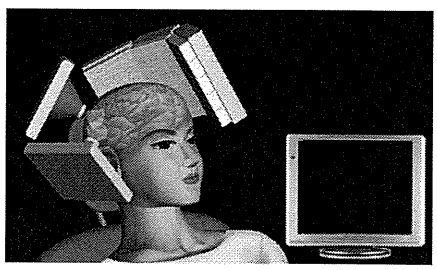

Figure 1. Large field of view detector for imaging whole brain and smaller field of view detectors for imaging ROIs.

As has been noted, with a small object-to-detector distance, both sensitivity and resolution of pinholes are better than that of the parallel-hole collimator [1]. However, the advantage is guaranteed at the expense of a small field of view. Imaging with a high resolution small field of view camera provides truncated projections. The reconstruction of these projections involves determining the solution to the interior problem in local tomography. The interior problem in medical imaging refers to the situation where the region-of-interest (ROI) is totally contained within the object. For instance, in SPECT, the interior problem happens when the projections passing through the region outside the ROI are truncated due to a small field-of-view detector or a short detector-to-object distance in the case of converging collimation. The interior problem has been

Manuscript received November 21, 2010. This work was supported by NIH under Grant No.R01EB00121, by the Director, Office of Science, Office of Biological and Environmental Research of the US Department of Energy under contract DE-AC02-05CH11231 and by the Grant for Translational Research from the Ministry of Health, Labour and Welfare (MHLW), Japan.

Q. Huang is with the Shanghai Jiao Tong University, Shanghai, China (e-mail: huangjone@yahoo.com).

T. Zeniya and H. Iida are with the National Cardiovascular Center Research Institute, Suita, Osaka, Japan.

H. Kudo is with University of Tsukuba, Tsukuba, Japan.

G. T. Gullberg is with the Lawrence Berkeley National Laboratory, Berkeley CA USA.

studied for some time [2]. Recently, it was proven that the solution is unique and stable in computed tomography (CT) if a small region in the ROI is known *a priori* [3-8]. Inspired by these works, the first author has presented some work on interior problem in SPECT imaging [9-10]. Previous work was performed analytically. In this paper the SPECT interior reconstruction problem is solved using an iterative algorithm.

The paper is organized as follows: Section II shows the method we used to simulate the combined parallel-hole and pinhole collimated imager and the algorithm to reconstruct the pinhole data. The result of a numerical simulation is presented in Section III where comparisons are made to illustrate the quantitation improvement with the camera. Then the conclusion is given in Section IV.

II. METHODS

We performed a simulation using the digital XCAT brain phantom [11]. The phantom was stored in a 3-dimensional volume with each voxel being $(2mm)^3$. The center of the volume was assumed to be the origin of the global coordinate system. One slice of the phantom is shown in Fig. 2.

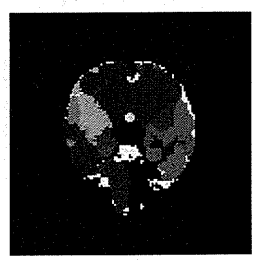

Fig. 2. The original XCAT phantom.

The large field of view parallel-hole collimated detector was simulated to revolve around the brain and acquire data every 5 degrees over half a circle. The detector bin was 0.28 cm along the transaxial direction and 0.2 cm along the axial direction. Poisson noise was manually added to the data to give a noise level such that the total counts of each slice summed to 10^7. The filtered backprojection algorithm was applied to the simulated projection data to reconstruct a volumetric image. Fig. 3 gives an example of one slice of the reconstructed low resolution volume. The image was interpolated and smoothed and was later used as the initial image and the prior information in the reconstruction of the pinhole data.

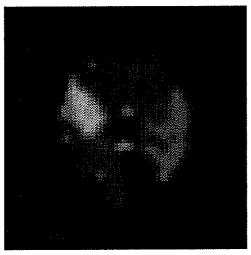

Fig. 3. The reconstructed image from parallel-hole projection data.

The pinhole collimator is shown in Fig. 4. It had a circular aperture with a radius of 0.5 mm and a knife edge with an opening angle of $\pi/3$. When the detector was localized close to the object, the projections were truncated as in Fig. 5. In the figure, the detector bin was 1.6 mm. The 2-dimensional detector plane had an area of 22.5×22.5 cm^2. In the simulation, pinhole collimated detector was assumed to be revolving to acquire 90 projections over a circle.

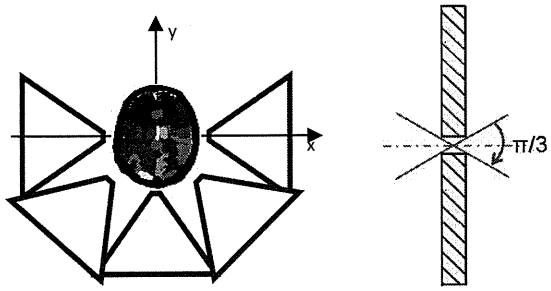

Fig. 4. The pinhole collimator. The pinhole is circular aperture with a radius of 0.5mm and a knife edge with an opening angle of $\pi/3$.

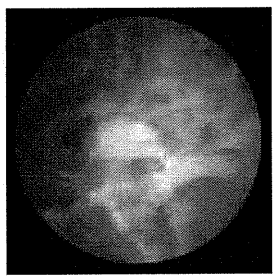

Fig. 5. Truncated projection data acquired by the pinhole collimated detector.

The reconstruction solved a linear system of equations $p=Af+noise$ for f which maximizes *a posteriori* probability $P(f|p)$. Since the *a posteriori* probability is

the product of the likelihood and the prior probability, the cost function can be expressed in two terms:

$$\Psi = -L(p \mid f) - \ln(\Phi(f)),$$

where the first term comes from the likelihood and the second term from the prior. Using the Gibbs prior

$$\Phi(f) = \frac{1}{Z} e^{-\beta U(f)},$$

the estimate was determined using the following procedure in a one-step-late algorithm [12]:

$$f_i^{new} = f_i^{old} \frac{\sum_j a_{ji} \frac{p_j}{\sum_{i'} a_{ji'} f_{i'}^{old}}}{\sum_j a_{ji} + \gamma^2 \frac{\partial}{\partial f_i} U(f^{old})}. \quad (1)$$

In this study, the energy term U(f) broke into two terms in the iteration step: one was a total variation penalty to account for the smoothness, the other included the prior information. Hence the procedure was

$$f_i^{new} = \frac{f_i^{old} \sum_j a_{ji} \frac{p_j}{\sum_{i'} a_{ji'} f_{i'}^{old}}}{\sum_j a_{ji} + \gamma_1^2 \frac{\partial}{\partial f_i} U_1(f^{old}) + \gamma_2^2 \frac{\partial}{\partial f_i} U_2(f^{old}, f_p)}$$

where γ_1 and γ_2 are regularization parameters. The first energy term U_1 utilized the total variation [13] of the reconstructed image. The second energy term was the distance between the estimate and the prior image f_p within the region of interest:

$$U_2(f^{old}, f_p) = \sqrt{\sum_{i \in ROI} (f^{old}(i) - f_p(i))^2}.$$

III. Results

In the simulation the pinhole data were acquired with truncation, resulting in reconstructing an interior problem. Efforts should be made to correct for the effect of this problem. Otherwise degradation is evident as shown in Fig. 6.

In this work, we used the low resolution image obtained by the large field of view detector first as the initial estimate in the iterative reconstruction of the pinhole data. Also, the low resolution image provided a priori information for the reconstruction of the interior problem.

The result is shown in Figs. 7 and 8. In this study, the L2 norm distance from the reconstructed image to the prior image was used in the penalty term. The image quality of the central part, which was the region of interest, was improved. The vertical and horizontal profiles crossing the center are shown in Fig. 8. From the profiles we see that the details of the image are more distinct by reconstructing both parallel-hole projection data and pinhole projection data; for instance, the details indicated by the arrows in Fig. 8.

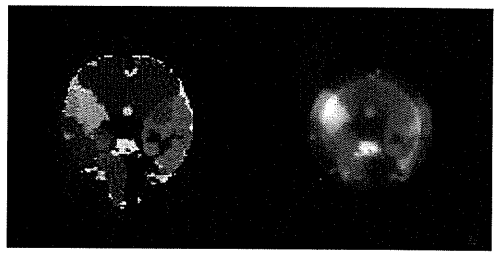

Fig. 6. Truncation effect. In both simulations, the pinhole collimated detector rotates around the object to acquire 90 views of projections and the same MAP estimate was performed with total variation regularization. The left image shows the result when there is no truncation and the right image shows the result with truncation. Degradation is evident in the right image due to the lack of correction for the interior reconstruction problem.

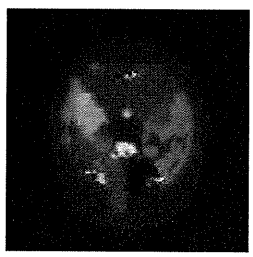

Fig. 7. Reconstructed image from pinhole data with interior problem and limited angular sampling. MAP estimate with regularization is applied.

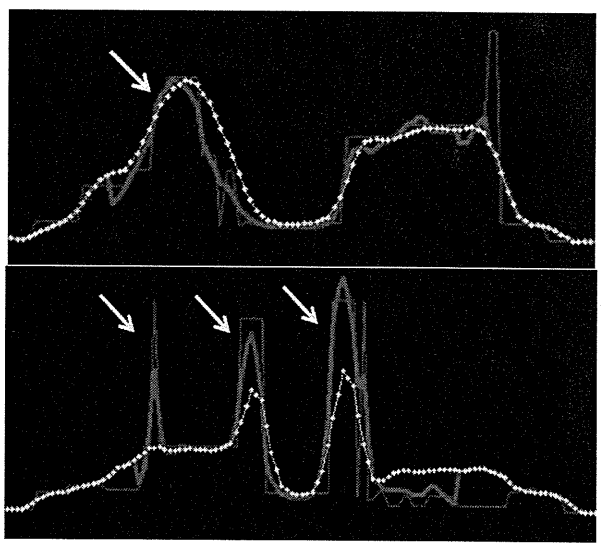

Fig. 8. Vertical and horizontal profiles crossing the center of the image. The purple solid line (thin) indicates the original phantom. The yellow dot-dash line is for the reconstructed image (Fig. 3.) from parallel-hole collimated data. While the red solid line (thick) is for the reconstructed image in Fig. 7.

IV. Conclusion

The combination of a large field of view parallel-hole collimated detector and smaller field of view high resolution pinhole detectors improves the quantitation in simulated brain imaging. It makes use of the high sensitivity of the pinhole collimator while compensates for the degradation in the reconstructed image due to the interior reconstruction problem caused by the small field of view of the pinhole collimator. This work will be verified through phantom imaging studies and patient imaging studies used to diagnose brain ischemia.

References

[1] R. J. Jaszczak, J. Li, H. Wang, M. R. Zalutsky, and R. E. Coleman, "Pinhole collimation for ultra-high-resolution, small-field-of-view SPECT," *Phys. Med. Biol.*, vol. 39, pp. 425-437, 1994.

[2] F. Natterer, *The Mathematics of Computerized Tomography* (SIAM), 1986.

[3] G. Wang, Y. Ye and H. Yu, "General VOI/ROI reconstruction methods and systems using a truncated Hilbert transform," Patent disclosure submitted to Virginia Tech. Intellectual Properties on May 15 2007.

[4] Y. Ye, H. Yu, and G. Wang, "Exact interior reconstruction with cone-beam CT," *Int. J. Biomed. Imaging,* Article ID. 10693, 2007.

[5] Y. Ye, H. Yu, Y. We and G. Wang, "A general local reconstruction approach based on a truncated Hilbert transform," *Int. J. Biomed. Imaging*, Article ID. 63634, 2007.

[6] Y. Ye, H. Yu, and G. Wang, "Exact interior reconstruction from truncated limited-angle projection data," *Int. J. Biomed. Imaging*, Article ID. 427987, 2008.

[7] M. Courdurier, F. Noo, M. Defrise and H. Kudo, "Solving the interior problem of computed tomography using a priori knowledge," *Inverse Problems*, vol. 24, pp. 065001, 2008.

[8] H. Kudo, M. Courdurier, F. Noo, and M. Defrise, "Tiny a proiri knowledge solves the interior problem in computed tomography," *Phys. Med. Bio.*, vol. 53, pp. 2207-2231, 2008.

[9] Q. Huang and G. T. Gullberg, "Exact Reconstruction from Uniformly Attenuated Truncated SPECT Projection Data with Tiny a Priori Knowledge," IEEE Nuclear Science and Medical Imaging Conference, Oct 25-31, 2009, Orlando.

[10] Q. Huang, T. Zeniya, H. Kudo, H. Iida, G. T. Gullberg "Interior SPECT reconstruction problem with tiny a proiri knowledge – an application for high resolution pinhole brain imaging," Proceedings of Fully 3D Meeting and HPIR Workshop, Sep. 5-10, 2009, Beijing, China, pp. 358-361.

[11] W. P. Segars and B. M. W. Tsui, "MCAT to XCAT: the evaluation of 4-D computerized phantoms for imaging research," Proceedings of the IEEE, vol. 97, No. 12, 2009.

[12] P. J. Green, "Bayesian reconstructions from emission tomography data using a modified EM algorithm," *IEEE Transactions on Medical Imaging*, vol. 9, pp 84-93, 1990.

[13] V. Y. Panin, G. L. Zeng, and G. T. Gullberg, "Total variation regulated EM algorithm," IEEE Transactions on Nuclear Science, vol. 46, pp. 2202-2210, 1999.

Eur J Nucl Med Mol Imaging (2010) 37:377–385
DOI 10.1007/s00259-009-1262-2

ORIGINAL ARTICLE

Quantification of regional myocardial oxygen metabolism in normal pigs using positron emission tomography with injectable ^{15}O-O_2

Takashi Temma · Hidehiro Iida · Takuya Hayashi · Noboru Teramoto · Youichiro Ohta · Nobuyuki Kudomi · Hiroshi Watabe · Hideo Saji · Yasuhiro Magata

Received: 27 April 2009 / Accepted: 10 August 2009 / Published online: 4 September 2009

Abstract
Purpose Although ^{15}O-O_2 gas inhalation can provide a reliable and accurate myocardial metabolic rate for oxygen by PET, the spillover from gas volume in the lung distorts the images. Recently, we developed an injectable method in which blood takes up ^{15}O-O_2 from an artificial lung, and this made it possible to estimate oxygen metabolism without the inhalation protocol. In the present study, we evaluated the effectiveness of the injectable ^{15}O-O_2 system in porcine hearts.
Methods PET scans were performed after bolus injection and continuous infusion of injectable ^{15}O-O_2 via a shunt between the femoral artery and the vein in normal pigs. The injection method was compared to the inhalation method. The oxygen extraction fraction (OEF) in the lateral walls of the heart was calculated by a compartmental model in view of the spillover and partial volume effect.
Results A significant decrease of lung radioactivity in PET images was observed compared to the continuous inhalation of ^{15}O-O_2 gas. Furthermore, the injectable ^{15}O-O_2 system provides a measurement of OEF in lateral walls of the heart that is similar to the continuous-inhalation method (0.71 ± 0.036 and 0.72 ± 0.020 for the bolus-injection and continuous-infusion methods, respectively).
Conclusion These results indicate that injectable ^{15}O-O_2 has the potential to evaluate myocardial oxygen metabolism.

Keywords Myocardial oxygen metabolism · PET · Pig · OEF · Injectable ^{15}O-O_2

T. Temma · H. Saji
Department of Patho-Functional Bioanalysis,
Graduate School of Pharmaceutical Sciences, Kyoto University,
Kyoto, Japan

H. Iida · T. Hayashi · N. Teramoto · Y. Ohta · N. Kudomi · H. Watabe
Department of Investigative Radiology,
National Cardiovascular Center Research Institute,
Osaka, Japan

Y. Magata (✉)
Laboratory of Genome Bio-Photonics,
Photon Medical Research Center,
Hamamatsu University School of Medicine,
1-20-1 Handayama,
Hamamatsu 431-3192, Japan
e-mail: magata@hama-med.ac.jp

Introduction

In the myocardium, fatty acid or glucose is used to produce energy by aerobic metabolism. Oxygen is one of the most important substrates closely related to the aerobic metabolism in the TCA cycle; thus, oxygen metabolism should be a direct reflection of myocardial metabolism of these substrates. Therefore, there has been considerable interest in the development of a method to quantify oxygen metabolism in the myocardium.

Recently, ^{11}C-acetate has been used for this purpose [1–5]. ^{11}C-acetate is taken up by the mitochondria and metabolically converted into acetyl-CoA. It then enters the TCA cycle and is transformed to ^{11}C-CO_2, which is cleared rapidly from the myocardium. Thus, the clearance pharmacokinetics reflects oxygen metabolism in the myocardium. However, the quantification of oxygen metabolism using ^{11}C-acetate is quite difficult because of various intermediary compounds.

The use of ^{15}O-O_2 gas inhalation and PET scanning can provide a quantitative myocardial metabolic rate for oxygen ($MMRO_2$) [6, 7]. The tracer kinetic model used is based on that originally proposed to describe the behavior of ^{15}O-O_2 in brain tissue [8, 9]. However, the direct translation of the

compartmental model for the brain to the heart is not permitted, because subtraction for spillover from gas volume in addition to that from the blood pool is needed. A previous study demonstrated that the gas volume can be accurately estimated from the transmission scan data; thus, this technique did not require additional emission scanning for estimating the quantitative gas volume images [6, 7]. However, gaseous radioactivity in the lung during the inhalation of ^{15}O-O_2 gas is too high in comparison to other regions. Subtraction for this contribution is straightforward and accurate using the transmission scan-derived gaseous volume images, but the lung radioactivity degraded image quality in the estimated $MMRO_2$ images.

As an alternative to gas inhalation, we recently developed a method to prepare an injectable form of ^{15}O-O_2. This was accomplished by exposing pre-collected blood to ^{15}O-O_2 gas using a small artificial lung system resulting in a maximum yield of 130 MBq/ml. We demonstrated that cerebral oxygen metabolism could be estimated in normal and ischemic rats using injectable ^{15}O-O_2 [10–12]. This technique has the potential of avoiding the inhalation protocol.

The aim of the present study was therefore to test the feasibility of using the injectable ^{15}O-O_2 oxygen system for estimating myocardial oxygen metabolism in pigs. The injection method was compared to the inhalation method to determine if the injection method resulted in a reduction of lung radioactivity, an improved image quality, a more accurate estimate of myocardial oxygen metabolism, and an improved signal-to-noise ratio.

Materials and methods

Theory

^{15}O-Oxygen was administered by IV injection or inhalation and was carried as ^{15}O-hemoglobin by blood to peripheral tissues including the myocardium, where it was converted to ^{15}O-water (^{15}O-H_2O_{met}) through aerobic metabolism. The increased distribution volume of ^{15}O-H_2O_{met}, represented by the exchangeable water space of tissue, causes delayed removal of radioactivity. This allows the definition of an appropriate model and equations to be derived for the calculation of a regional myocardial metabolic rate for oxygen ($rMMOR_2$) and regional oxygen extraction fraction (rOEF). Previous studies demonstrated that these calculations were similar to those used for estimating cerebral blood flow and oxygen metabolism and require the measurement of regional myocardial blood flow (rMBF) and a correction for spillover of activity from the vascular pools and the pulmonary alveoli [6, 7]. rMBF was measured by the ^{15}O-H_2O injection technique [13]. Activity in the vascular pools of the heart chambers and the lung was evaluated with a conventional measurement of blood volume using ^{15}O-CO, and activity in the pulmonary alveoli was evaluated with an unconventional and indirect measurement of gas volume obtained from the transmission scan. Furthermore, the existence of recirculating ^{15}O-H_2O_{met} in the blood freely accessible to the myocardium was taken into consideration.

The differential equation describing the myocardial kinetics after administration of ^{15}O-O_2 can be written as follows:

$$\frac{dC^{myo}(t)}{dt} = OEF \cdot f \cdot A_o(t) + f \cdot A_w(t) - \left(\frac{f}{p} + \lambda\right) C^{myo}(t) \quad (1)$$

where $C^{myo}(t)$ designates the true radioactivity concentration in the myocardium at time t, f is myocardial blood flow, $A_O(t)$ is the ^{15}O-O_2 radioactivity concentration in arterial blood, $A_W(t)$ is the ^{15}O-H_2O radioactivity concentration in arterial blood, p is the myocardium/blood partition coefficient of water, and λ is the physical decay constant of O-15.

Solving Eq. (1) in terms of $C^{myo}(t)$ gives:

$$C^{myo}(t) = OEF \cdot f \cdot A_o(t) * e^{-\left(\frac{f}{p}+\lambda\right)\cdot t} + f \cdot A_w(t) * e^{-\left(\frac{f}{p}+\lambda\right)\cdot t} \quad (2)$$

where the asterisk denotes the convolution integral. During steady-state conditions under the continuous administration of ^{15}O-O_2, the following relationship holds:

$$C^{myo} = \frac{OEF \cdot f \cdot A_o + f \cdot A_w}{\left(\frac{f}{p} + \lambda\right)} \quad (3)$$

In the actual PET studies, the spillover from vascular pools and pulmonary alveoli and the partial volume effect should be taken into consideration [14]. Then, the measured radioactivity concentration in the region of interest (ROI) in the myocardium ($R^{myo}(t)$) can be expressed as:

$$\begin{aligned} R^{myo}(t) = {} & \alpha \cdot C^{myo}(t) \\ & + (V_B^{myo} \cdot A_t(t) - \alpha \cdot F_{Vein} \cdot OEF \cdot A_o(t) - \alpha \cdot F_{Vein} \cdot A_w(t)) \\ & + V_G^{myo} \cdot C_{gas}(t) \end{aligned} \quad (4)$$

where α denotes the myocardial tissue fraction, V_B^{myo} is the myocardial blood volume, $A_t(t)$ is the total O-15 radioactivity concentration in arterial blood, F_{vein} is the microscopic venous blood volume, V_G^{myo} is the gas volume in the myocardial ROI and $C_{gas}(t)$ is the O-15 radioactivity concentration in V_G^{myo}.

With the bolus injection or infusion methods using an artificial lung system, the radioactivity in the pulmonary alveoli is expected to be negligible in comparison with the inhalation method. Thus, Eq. (4) can be converted to:

$$R^{myo}(t) = \alpha \cdot C^{myo}(t) + (V_B^{myo} \cdot A_t(t) - \alpha \cdot F_{Vein} \cdot OEF \cdot A_o(t) - \alpha \cdot F_{Vein} \cdot A_w(t)) \quad (5)$$

Subjects

In this study, four healthy miniature pigs (22–30 kg) were used. The pigs were anesthetized by IM injection of ketamine and xylazine followed by continuous infusion of propofol (5 mg/kg/h). The animals were then placed in the supine position on the bed of the PET scanner. All experimental procedures were approved by the local animal welfare committee.

Injectable ^{15}O-O_2 preparation

In the "injection" study, injectable ^{15}O-O_2 was used. Injectable ^{15}O-O_2 was prepared as described previously [10–12]. In brief, part of an infusion line kit (Terumo Corporation, Tokyo, Japan) and an artificial lung 18 cm in length (Senko Medical Instrument Mfg Co. Ltd., Tokyo, Japan) were connected using silicone tubing to make a closed system. Then, venous blood collected from a pig, which was used in the following PET studies, was added to the system and circulated (100 ml/min) by a peristaltic pump, followed by introduction of ^{15}O–O_2 gas (~7,000 MBq/min/433 ml) into the artificial lung for 15 min to prepare injectable ^{15}O-O_2 (5.6–60.7 MBq/ml).

In the "continuous infusion" study, the left femoral artery and right femoral vein were both cannulated. The two cannulas from the artery and the vein were connected to the opposite sides of an artificial lung to create a femoral shunt. The blood flow in the shunt was aided by a peristaltic pump (30–50 ml/min). ^{15}O-O_2 gas (~7,000 MBq/min/433 ml) was continuously introduced into the artificial lung.

PET protocol (Fig. 1)

The PET scanner was an ECAT EXACT HR (CTI/Siemens) [15], which has an imaging field of view (FOV) of 55 cm in diameter and 15 cm in axial length. The spatial resolution of the scanner is 5.8 mm in full width at half maximum at the center of the FOV.

After obtaining a 20-min transmission scan for attenuation correction and gas volume estimation, the blood pool image was obtained with a 4-min PET scan after the pigs inhaled 2.7 GBq ^{15}O-CO for 30 s. Arterial blood samples were taken every minute during the ^{15}O-CO scanning, and

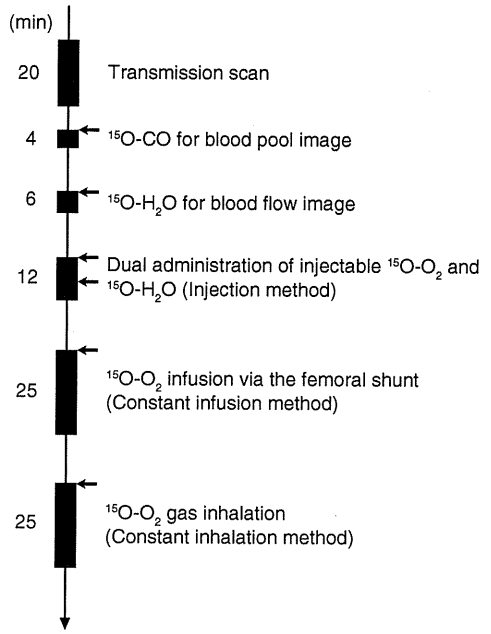

Fig. 1 Outline of the PET imaging study. The interval between scans was more than 15 min to allow for physical decay of O-15 radioactivity to background levels

the radioactivity concentration in the whole blood was measured with a NaI well-type scintillation counter calibrated against the PET scanner. Subsequently, ^{15}O-water was injected into the right femoral vein for 30 s at an infusion rate of 10 ml/min (injected radioactivity was about 1.11 GBq). Immediately after injection of ^{15}O-water, 26 dynamic frames (12×5 s, 8×15 s and 6×30 s) of PET data were acquired for 6 min.

Furthermore, two PET scans were successively performed after the IV injection of ^{15}O-O_2 (5.6–60.7 MBq/ml) for 30 s at an injection rate of 20–80 ml/min for the "injection" study, and by the continuous ^{15}O-O_2 gas infusion through the artificial lung in the femoral shunt for the "continuous infusion" study. In the "injection" study, 52 dynamic frames (12×5 s, 8×15 s, 6×30 s, 12×5 s, 8×15 s and 6×30 s) of PET data were acquired for 12 min, and 1.11 GBq of ^{15}O-water was injected IV for 30 s at 10 ml/min starting at 6 min after the administration of IV ^{15}O-O_2 according to the dual administration protocol we developed previously [16]. In the "continuous infusion" study, 26 dynamic frames (10×30 s, 5×60 s, 1×600 s and 10×30 s) were acquired for 25 min, and the 600-s frame was used for steady-state analysis.

Another PET scan was performed by ^{15}O-O_2 gas inhalation in one of the four pigs in the same protocol as the "continuous infusion" study. This was the "continuous inhalation" study. The interval between scans was more

than 15 min to allow for physical decay of O-15 radioactivity to background levels. All acquisitions were obtained in the two-dimensional mode (septa extended).

Data analysis

A filtered back-projection algorithm with a 6-mm Gaussian filter was used for image reconstruction. The reconstructed images had a matrix size of 128 × 128 × 47 and a voxel size of 1.84 × 1.84 × 3.38 mm, and all image data sets were resliced into short-axis images across the left ventricle [13].

Myocardial blood flow

rMBF was calculated from the injection of ^{15}O-H_2O by fitting the myocardial and arterial time-activity curve data to a single-tissue-compartment model that implemented corrections for partial-volume effects by introducing the tissue fraction. In addition, the model was corrected for spillover from the left ventricular (LV) chamber into the myocardial ROI by introducing the arterial blood volume [13]. In these experiments, the time-activity curves generated from large ROIs placed in the LV chamber were used as the input function.

Regional oxygen extraction fraction

In the "injection" study, rOEF was calculated according to Eqs. (2) and (5). In these formulations, F_{vein} was assumed to be 0.10 ml/g tissue and p was fixed at 0.90 ml/g. The blood volume image obtained from the ^{15}O-CO scan was used for the determination of V_B^{myo}. The value of $A_t(t)$ was obtained from the LV radioactivity concentration measured from the PET data set with small LV ROIs to minimize spillover from the myocardium. The calculation for the estimation of recirculating ^{15}O-H_2O was performed as previously described [16]. For the "continuous infusion" and "continuous inhalation" studies, in which a 600-s frame was regarded as steady-state, Eqs. (3) and (5) or Eqs. (3) and (4) were used for calculating rOEF, respectively.

Results

Table 1 summarizes the conditions of animals during the PET studies. The parameters were all within the physiologic range.

Figure 2 demonstrates the dynamic images obtained in the "injection", "continuous infusion", and "continuous inhalation" studies. With the injection and continuous-infusion methods, the right ventricle on the left side and the vena cava on the lower side were well delineated, whereas the left ventricle was moderately shown on the right side. The 16th frame (600~1,200 s after the initiation), which was used for steady-state analysis with the continuous-infusion method, was visibly distinct compared with all of the frames obtained with the injection method. However, with the continuous-inhalation method, neither ventricle could be depicted because of high radioactivity in the lung on the right and lower-side images.

The radioactivity in the blood pool obtained by ^{15}O-CO PET (Fig. 3g) and the gaseous volume estimated by inverse transmission data (Fig. 3h) were subtracted from the raw PET images (16th frame) with the continuous-inhalation and continuous-infusion methods, respectively (Fig. 3c and f). Both methods clearly delineated the myocardium after subtraction in comparison to the blood flow image (Fig. 3i). However, the continuous-inhalation method showed salient radioactivity on the lateral wall (Fig. 3c), whereas the continuous-infusion method showed only modest radioactivity in the myocardium (Fig. 3f). It is also notable that there was considerable radioactivity in the right ventricle with the continuous-infusion method even after the subtraction (Fig. 3f).

To further examine the differences between the continuous-infusion and continuous-inhalation methods, time-radioactivity curves during the PET scans were taken from four ROIs: the left ventricle (LV), right ventricle (RV), myocardium (Myo), and lung (Fig. 4). At the steady-state frame (600~1,200 s), the continuous-infusion method showed higher radioactivity in the RV and LV than in the myocardium (Fig. 4a), whereas the radioactivity of these regions was similar with the continuous-inhalation method (Fig. 4b). The radioactivity in LV was about two-thirds of that in RV in Fig. 4a, indicating that measurable radioactivity was excreted through the lung even after the femoral administration of ^{15}O-O_2. The lung excretion was also observed on the blood-subtracted image (Fig. 3e). Actually, there was significant radioactivity in the lung (Fig. 4a), although that was the lowest among the four ROIs. In contrast, the radioactivity in the myocardium was the lowest among the four ROIs with the continuous-inhalation method

Table 1 Physiological parameters of pigs during the PET studies

	pH	pCO_2 (mmHg)	pO_2 (mmHg)	tHb (g/dl)	O_2Sat (%)	HR (bpm)	BP (mmHg)	
							Diastolic	Systolic
Average	7.46	40.3	125.8	12.8	97.7	85	97.8	125.2
SD	0.032	2.51	16.69	1.30	1.83	19.5	10.4	19.3

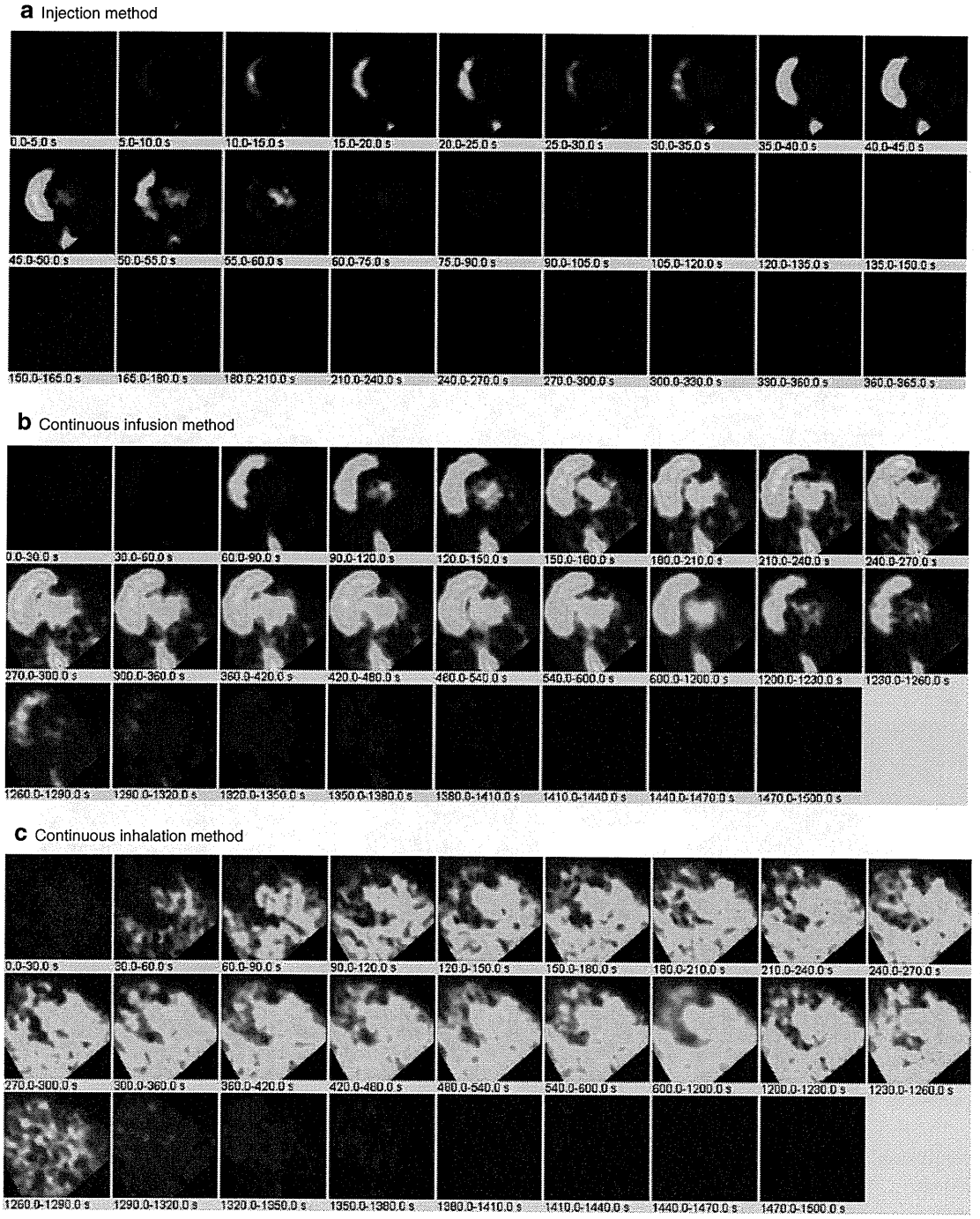

Fig. 2 PET images obtained in (**a**) the injection method, (**b**) the continuous-infusion method with injectable ^{15}O-O_2, and (**c**) the continuous-inhalation method with ^{15}O-O_2 gas

(Fig. 4b). The heart-to-lung radioactivity ratios were calculated from Fig. 4 for the quantitative estimation of image quality; the continuous-infusion method provided a ratio of 1.38±0.24, whereas the ratio was less than one with the continuous-inhalation method.

Table 2 shows the quantitative OEF values in the lateral wall obtained by the injection, continuous-infusion, and continuous-inhalation methods. These OEF values were consistent among the three methods.

Figure 5 represents the noise equivalent counts (NEC) standardized by the total counts detected by the PET scanner. Although the injection method tended to show rather high values, there was no significant difference between the values obtained by the injection and

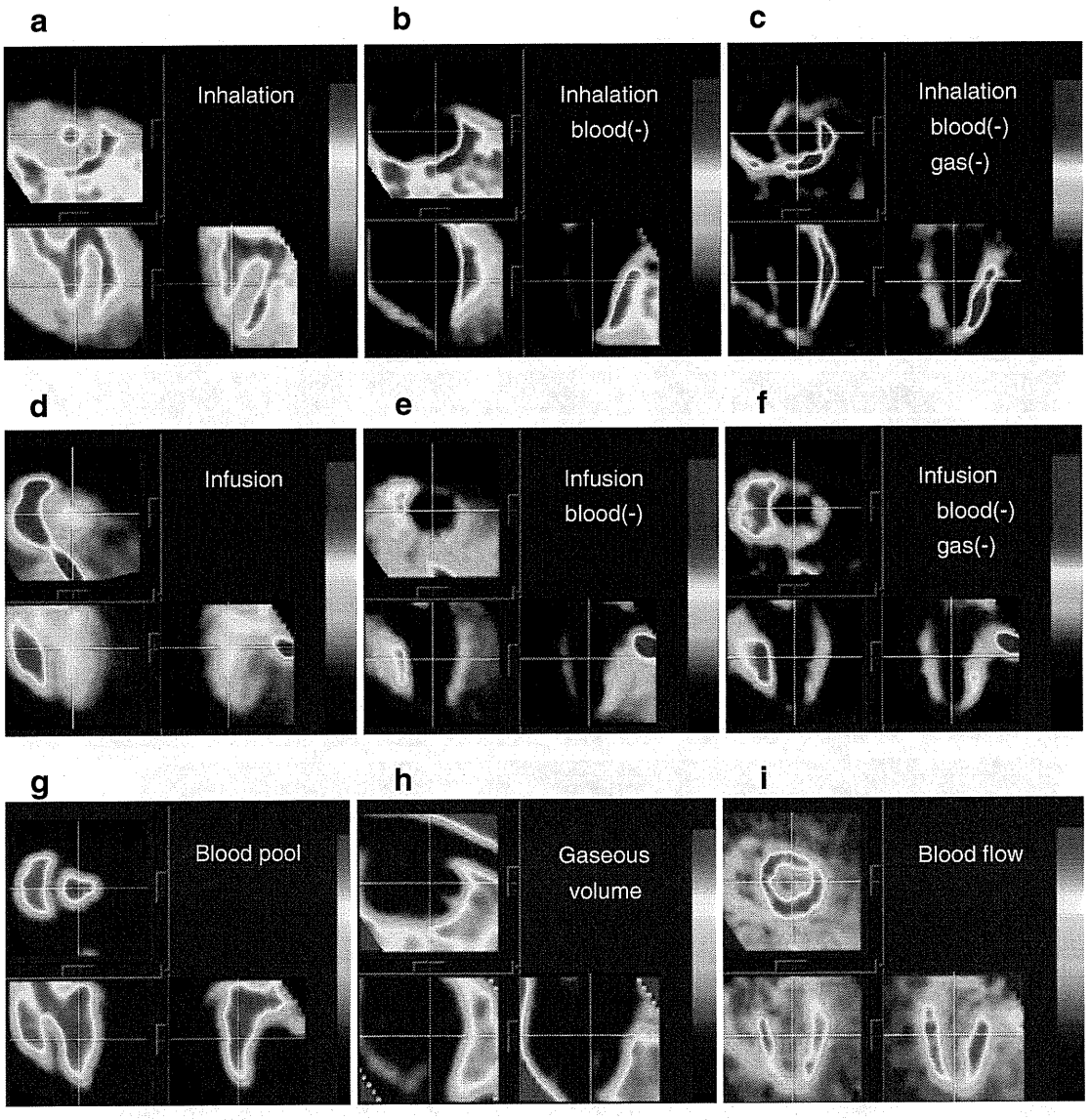

Fig. 3 PET images obtained in the study are shown. The 16th frame (steady-state frames) of the continuous-inhalation method and the continuous-infusion method are shown in (**a**) and (**d**), respectively. The 'blood-subtracted' images shown in (**b**) and (**e**) were created by subtraction of the blood-pool image by ^{15}O-CO (**g**) from (**a**) and (**d**). The 'blood- and gas-subtracted' images shown in (**c**) and (**f**) were created by the successive subtraction of the gaseous image (**h**) from (**b**) and (**e**). The myocardial blood flow image is also shown in (**i**)

continuous-infusion methods as determined by a Mann Whitney *U*-test.

Discussion

In previous studies, we showed the usefulness of the injectable ^{15}O-O_2 system for estimating cerebral oxygen metabolism in small animals such as rats under normal or ischemic conditions [10–12]. Injectable ^{15}O-O_2 replaced the inhalation protocol and radioactive ^{15}O-O_2 was administered via the tail vein. Thus, injectable ^{15}O-O_2 could abolish the artifact from the high radioactivity in the inhalation tube that distorts the PET images, especially in small animals. We considered that the concept could also be utilized in the hearts of large animals. Therefore, in the present study, we tested the feasibility of an injectable ^{15}O-O_2 system for estimating myocardial oxygen metabolism in normal pigs. In addition, since a shunt between the femoral artery and vein can be created in pigs but not in small animals, continuous infusion via the femoral shunt was also performed to achieve a constant and reliable delivery of radioactivity to the heart.

Dynamic PET scans showed a large difference in the radioactivity distribution among the three methods. Since the labeling efficiency to prepare injectable ^{15}O-O_2 was

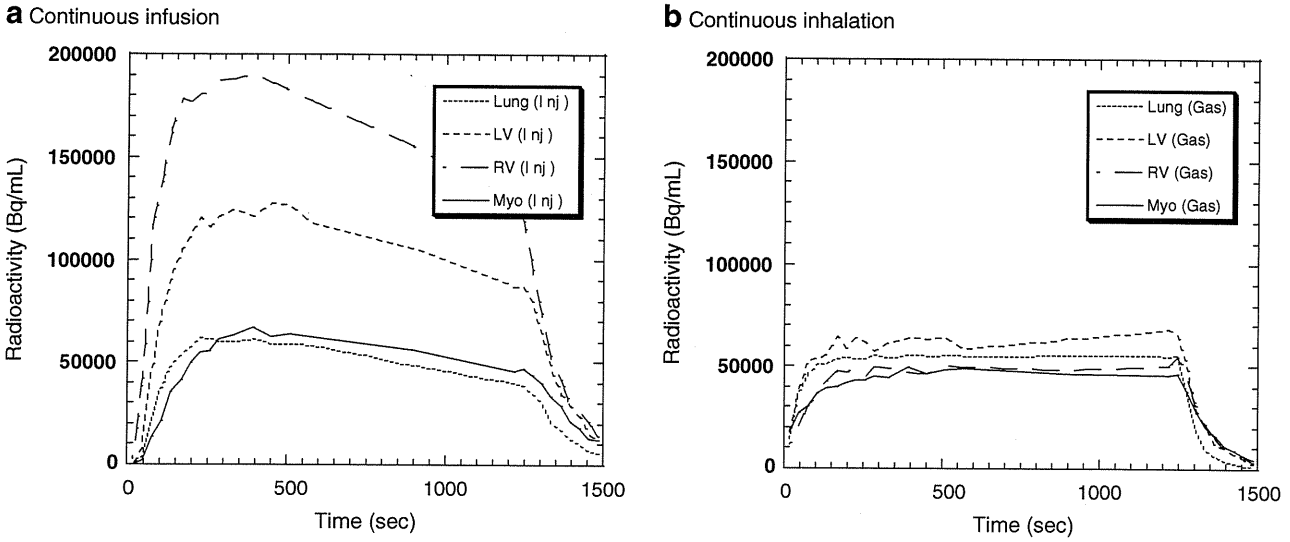

Fig. 4 Time-activity curves from the left ventricle (*LV*), the right ventricle (*RV*), the myocardium (lateral wall, Myo) and a lung region with the continuous-infusion method (**a**) and the continuous-inhalation method (**b**). The supply of radioactivity was started at time 0 s and stopped at 1,200 s. The 16th frame for the steady-state analysis was 600–1,200 s

lower with pig blood (ca. 61 MBq/ml at most) than with the blood of rats and humans (130 MBq/ml), the injection method provided rather obscure images. With the injection and continuous-infusion methods, the radioactivity in the lung was dramatically reduced in comparison to the continuous-inhalation method, since the heart-to-lung ratio with the continuous-infusion method was about 40% higher than with the continuous-inhalation method. This finding suggested that the two methods that inject radioactivity via a vein are more useful for analyzing myocardial oxygen metabolism in pigs than the continuous-inhalation method. However, a distinct difference between radioactivity of the right and left ventricles was observed in the images and time-radioactivity curves after venous administration of ^{15}O-O_2, indicating a certain degree of excretion of the radioactivity by the lung. Therefore, the spillover from the pulmonary alveoli to the myocardium could not be omitted in the two methods with venous administration, and Eq. (4) was used for the OEF analysis, although the radioactivity in the lung was lower than that in the myocardium.

On the other hand, with the continuous-inhalation method, the radioactivity of the lung was in between the radioactivity in the RV and LV. This is curious because O-15 radioactivity was supplied from the inhalation tube and transferred from the lung to blood so that the radioactivity in the lung should have been the highest among the four ROIs. This may have been caused, in part, by inhomogeneous distribution of the radioactivity in the lung due to its structure in comparison with the myocardium and ventricles, and/or by artifacts from the lung to other

Table 2 OEF estimated by the three methods using injectable ^{15}O-O_2 or ^{15}O-O_2 gas

	OEF		
	Injection	Infusion	Inhalation
Pig. 1	0.70	0.72	
Pig. 2	0.67	0.72	
Pig. 3	0.71	0.74	
Pig. 4	0.76	0.69	0.72
Average	0.71	0.72	0.72
SD	0.036	0.020	

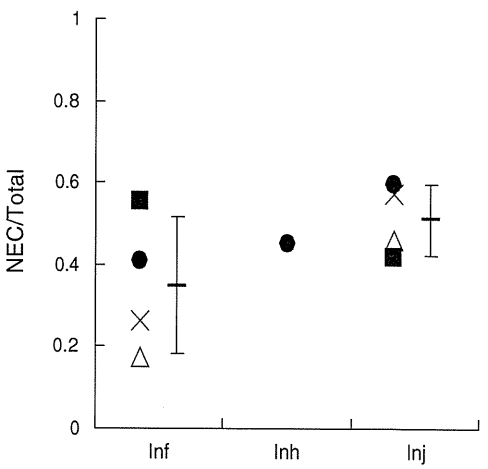

Fig. 5 The ratio of noise equivalent counts (*NEC*) to total counts in the total field of view of the PET scanner obtained with the continuous-infusion method (*Inf*), the continuous-inhalation method (*Inh*) and the injection method (*Inj*)